2020 IEEE/RSJ International Conference on Intelligent Robots and Systems (IROS)
October 25-29, 2020, Las Vegas, NV, USA (Virtual)

Extrinsic and Temporal Calibration of Automotive Radar and 3D LiDAR

Chia-Le Lee*, Yu-Han Hsueh*, Chieh-Chih Wang, Wen-Chieh Lin

***Abstract*— While automotive radars are widely used in most assisted and autonomous driving systems, only a few works were proposed to tackle the calibration problems of automotive radars with other perception sensors. One of the key calibration challenges of automotive planar radars with other sensors is the missing elevation angle in 3D space. In this paper, extrinsic calibration is accomplished based on the observation that the radar cross section (RCS) measurements have different value distributions across radar's vertical field of view. An approach to accurately and efficiently estimate the time delay between radars and LiDARs based on spatial-temporal relationships of calibration target positions is proposed. In addition, a localization method for calibration target detection and localization in pre-built maps is proposed to tackle insufficient LiDAR measurements on calibration targets. The experimental results show the feasibility and effectiveness of the proposed Radar-LiDAR extrinsic and temporal calibration approaches.**

***Index Terms*— Radar, LiDAR, Extrinsic Calibration, Temporal Calibration.**

I. Introduction

Sensor fusion is essential and critical to enhance and ensure the performance and reliability of the machine perception modules in assisted and autonomous driving. Both offline and online calibrations are the most critical procedures for sensor fusion. There have been a number of approaches and systems for accomplishing calibration between cameras, LiDARs and IMUs [1]–[7]. While automotive mmWave radars are widely used in assisted and autonomous driving, only a few works address calibration between radars and other perception sensors [8]–[13]. In this paper, we focus on both extrinsic and temporal calibration between a planar automotive radar and a 3D LiDAR. Fig. 1 shows the test vehicle with the sensors used in this work.

One of the most challenging issues in this extrinsic calibration setting is that planar radars only offer two dimensional geometric measurements and one dimensional radial velocity measurements but a rigid transformation between the coordinate systems of the planar radar and the 3D LiDAR must be estimated. To solve this issue, Peršić et al. [12], [13] proposed to use radar echo intensities, i.e., radar cross section (RCS) values to infer the missing dimension of the planar radar in which the transformations between a radar, a LiDAR and a camera could be estimated. As their data collection process is proceeded by driving a robot in front of the targets, and acquire data under the condition that the sensors and the target are both stationary, they are able to avoid the influence from the time delay between radar and LiDAR. However, temporal calibration is also essential and important for sensor fusion. Fig. 2 shows a mismatch of the radar measurements and the LiDAR measurements due to the time delay between the two sensors despite good extrinsic calibration.

Fig. 1. Sensors on the test vehicle. One Velodyne HDL-32E LiDAR and three Delphi ESR radars are used in this work.

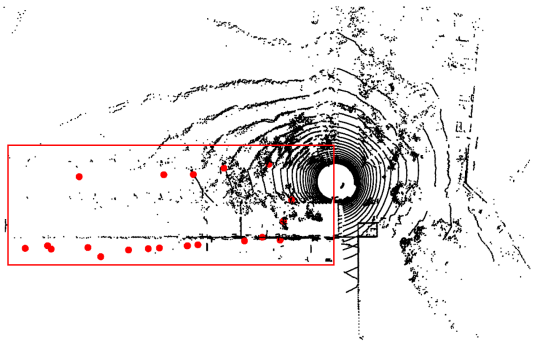

Fig. 2. The mismatch problem between radar measurements (red spheres) and LiDAR measurements (black points) due to the time delay.

Most of the recent works on temporal calibration between cameras, LiDAR or IMU are trajectory-alignment based approaches [14]–[18]. Following the same trajectory-alignment principles, we present an approach to accomplish temporal calibration between automotive radar and 3D LiDAR. While the motion and the trajectory estimation using radar are less accurate compared to cameras and IMU, a target-based approach is proposed. Due to the uncertainty of radar, rapid

*Authors have contributed equally and names are in alphabetical order.
Chia-Le Lee is with the Institute of Electrical and Computer Engineering, National Chiao Tung University, Hsinchu, Taiwan. E-mail: caleb.eed04@nctu.edu.tw
Yu-Han Hsueh is with the Institute of Electrical and Control Engineering, National Chiao Tung University, Hsinchu, Taiwan. E-mail: zero000.ece07g@nctu.edu.tw
Chieh-Chih Wang is with the Department of Electrical and Computer Engineering, National Chiao Tung University, and with the Mechanical and Mechatronics Systems Research Laboratories, Industrial Technology Research Institute, Hsinchu, Taiwan. E-mail: bobwang@ieee.org
Wen-Chieh Lin is with the Department of Computer Science, National Chiao Tung University, Hsinchu, Taiwan. E-mail: wclin@cs.nctu.edu.tw

(a) extrinsic calibration.

(b) temporal calibration.

Fig. 3. The targets are placed in an open area.

(a) Front view

(b) Back view

Fig. 4. Calibration target used in this paper: a triangular styrofoam board fixed in front of a corner reflector as it is invisible to radar.

motions are preferred during data collection for ensuring the time delay's observability. Since the time delay effect would be magnified at the long range objects, the targets are placed both at short range and long range as shown in Fig. 3(b). While radar can perceive the target at long range, LiDAR is unable to detect the target owing to sparse LiDAR measurements. Hence, a target localization approach is proposed for dealing with this issue.

The contributions of this paper are that: (1) A temporal calibration procedure is proposed to estimate the time delay accurately and efficiently in which the required sensor motion is analyzed. (2) Calibration target detection and localization in pre-built maps are applied. (3) This is the first work to address both extrinsic and temporal calibration problems of automotive radar and LiDAR to the best of our knowledge.

II. Establishing Correspondence

To calibrate radars and LiDARs, target that can induce reliable, distinguishable, and sensitive measurements from the two sensors is desirable. We adopt the same calibration target designed in [12], [13], which includes a corner reflector and a triangular styrofoam board as shown in Fig. 4. For radars, corner reflector's reflective characteristics ensure that it is easily detected; for LiDARs, a triangular styrofoam board is used to estimate the pose of the target. Since the styrofoam material is invisible to the radar, the corner reflector is placed behind the triangular styrofoam board as shown in Fig. 4(b) in which the radar and the LiDAR can perceive the target without mutual interference. The centers of the corner reflector and the triangular styrofoam board are well aligned and assumed at the same location. Accordingly, the target centers from radar and LiDAR measurements can be estimated and used to establish correspondences.

A. Estimating the target center from the radar measurements

A radar measurement includes the range to the center ${}^{r}r_{r}$ of the object and its azimuth angle ${}^{r}\phi_{r}$, where the left superscript represents it resides at the radar frame F_r; the right subscript means the measurement is derived from the radar. Besides, the RCS value δ_r, which represents the reflection intensity of the object, is also provided by the radar. Since the automotive radars do not provide vertical information of the object (i.e. the elevation angle is missing), for each radar measurement, there is a potential arc that the object can possibly reside in 3D space. When using radars for object detection and tracking, the projected point on the radar plane P_r (of elevation angle equals 0) is often used as the position of an object. When calibrating an automotive radar with a 3D LiDAR, the missing elevation angle would cause a non-negligible estimation error on vertical components of 6 DoF transformation. Nevertheless, the vertical components such as z-translation, pitch, and roll, can still be refined by taking RCS values into account. The details will be discussed in Section III-B. In our calibration setting, targets are stationary and tracked during the data collection process. At time t_i the measurement of the k-th target: ${}^{r}s_{rk}(t_i) = [{}^{r}r_{rk}(t_i) \ {}^{r}\phi_{rk}(t_i) \ ]$ with the RCS value $\delta_{rk}(t_i)$ can be collected for extrinsic and temporal calibration.

B. Estimating the target center from the LiDAR measurements

In contrast to radar's sparse measurements, LiDAR can provide dense 3D point measurements. However, the LiDAR measurements could still become sparse for objects located at long range, resulting in the decrease of the accuracy in target detection and pose estimation. In this work, the target center is estimated via LiDAR localization given the target pose with respect to the pre-built map rather than detecting the target center directly. By doing so, the target center can be estimated even it is far away from the LiDAR and the overlap of FoV between radar and LiDAR is not necessary. In the data collection process, it is only necessary to ensure the targets can be perceived by radar. The approach is divided into two steps:

1) Mapping and localization: By using the scan matching algorithm, e.g., Iterative Closest Point (ICP) [19] or Normal Distribution Transform (NDT) [20], a point cloud map of the environment with multiple calibration targets is built. After localization is done, the transformation ${}^{l}T_{m}(t_j)$ from the map frame F_m to the LiDAR frame F_l at time t_j can be computed.

2) Estimation of the target center: The target centers at each LiDAR scan are estimated by transforming target centers from the map frame F_m to the LiDAR frame F_l. To obtain the target centers in the map, a triangle model is defined and optimized to fit the edge points of the triangle board. In consequence, the pose of the target center is obtained. We denote the position of the k-th target in the map as ${}^{m}p_{lk}$, and the target center in the LiDAR frame at

time t_j can be estimated by the following equation:

$$^{l}p_{lk}(t_j) = {}^{l}T_m(t_j) \cdot^{m} p_{lk} \tag{1}$$

C. Correspondence establishment

In order to associate the data from the two sensors, the target centers from the LiDAR measurements are transformed into the radar frame by an initial approximate transformation ${}^{r}T_l$. Since different parameterization choices would cause different uncertainty on the refined parameters as elaborated in [13], the recommended parameterization is adopted. The transformation ${}^{r}T_l$ from F_l to F_r includes two parts: $[{}^{r}t_l \ {}^{l}\Theta_r]$, where ${}^{r}t_l = [t_x \ t_y \ t_z]$ and ${}^{l}\Theta_r = [\theta_z \ \theta_y \ \theta_x]$ denote the translation part from F_l to F_r, and rotation part from F_r to F_l. The Euler angle representation is used in the rotation part ${}^{l}\Theta_r$, where θ_z, θ_y, θ_x are yaw, pitch and roll, and the rotation matrix is given by:

$$R({}^{l}\Theta_r) = R_x(\theta_z)R_y(\theta_y)R_z(\theta_x) \tag{2}$$

The target center ${}^{l}p_{lk}(t_j)$ estimated from the LiDAR measurements is transformed to the radar frame as ${}^{r}p_{lk}(t_j)$:

$$^{r}p_{lk}(t_j) = {}^{r}T_l \cdot {}^{l}p_{lk}(t_j) \tag{3}$$

The radar measurements near ${}^{r}p_{lk}(t_j)$ within a predefined distance threshold are checked and the closest one is chosen as the target center estimation from radar. As a result, the radar-LiDAR correspondence is established. As the target centers from the radar measurements are described in the spherical coordinate system, ${}^{r}p_{lk}(t_j)$ is converted to the representation in spherical coordinate as ${}^{r}s_{lk}(t_j) = [{}^{r}r_{lk}(t_j) \ {}^{r}\phi_{lk}(t_j) \ {}^{r}\psi_{lk}(t_j)]$ for reprojection process in Section III-A and temporal calibration in Section IV. In addition, since the timestamps of radar measurements and LiDAR measurements are discrete and different, linear interpolation [21] is used to keep the correspondences built in the same timestamps. It should be noted that uncertainties in the map and the localization module could degrade the performance of target localization. The accuracy of the map and the localization approaches should be analyzed and could be further improved to obtain better calibration results. Once the correspondences between Radar and LiDAR measurements are established, extrinsic and temporal calibration could be accomplished using these correspondences.

III. Extrinsic Calibration

In this work, it is assumed that intrinsic calibrations of radar and LiDAR are achieved by the manufacturers, so we only need to focus on extrinsic and temporal calibration between radar and LiDAR. Following the work [12], [13], the extrinsic calibration can be formulated as a two-stage optimization problem including reprojection error optimization and RCS error optimization. In the reprojection error optimization, our method follows [12], [13]. Regarding the RCS error optimization, [13] represents the RCS-elevation dependence as a second-order polynomial and optimizes the squared distance between the measured RCS and expected RCS.

Our method proposes to use subsets of the correspondences along the elevation central and boundary planes that are determined with RCS values to optimize the squared distance between transformed LiDAR data and the corresponding plane. The details will be described in this section.

A. Reprojection Error Optimization

For readability, the reprojection error optimization is briefly described. In this stage, the current estimated extrinsic parameters are represented as a six degree-of-freedom (DoF) parameter set $c_p = [{}^{r}t_l \ {}^{l}\Theta_r]$. Accordingly, the LiDAR data ${}^{r}s_{lk}(t_i) = [{}^{r}r_{lk}(t_i) \ {}^{r}\phi_{lk}(t_i) \ {}^{r}\psi_{lk}(t_i)]$ for each correspondence can be obtained, and projected into the radar plane by ignoring the elevation angle ${}^{r}\psi_{l,i}$. Therefore, the reprojection error term is defined as the distance between projected LiDAR data and radar data on the radar plane in which ${}^{r}\psi_{lk}(t_i) = {}^{r}\psi_{rk}(t_i) = 0^\circ$:

$$\epsilon_{ik}(c_p) = \|p_r - p_l\| \tag{4}$$

where

$$p_r = \begin{bmatrix} {}^{r}r_{rk}(t_i)\cos({}^{r}\phi_{rk}(t_i)) \\ {}^{r}r_{rk}(t_i)\sin({}^{r}\phi_{rk}(t_i)) \end{bmatrix}, p_l = \begin{bmatrix} {}^{r}r_{lk}(t_i)\cos({}^{r}\phi_{lk}(t_i)) \\ {}^{r}r_{lk}(t_i)\sin({}^{r}\phi_{lk}(t_i)) \end{bmatrix}$$

The calibration parameters $\hat{c_p}$ are obtained by minimizing the cost function using the Levenberg-Marquardt (LM) algorithm implemented by the Ceres Solver [22]:

$$\hat{c_p} = \arg\min_{c_p}\Big(\sum_{i=0}^{N-1}\sum_{k=0}^{K-1}\epsilon_{ik}^2\Big), \tag{5}$$

where the cost function is the sum of the square of reprojection error across $N \times K$ correspondences.

B. RCS Error Optimization

Once reprojection error optimization is completed, the six calibration parameters are estimated. However, t_z, θ_y, θ_x would have higher uncertainty comparing with other parameters since the elevation angle is neglected in the projection process. Consequently, these three parameters are refined using RCS measurements.

The distribution of the RCS measurements δ_r's across 3D space has the following characteristics:

1) The radar measurements which are closer to the radar plane (i.e., elevation angle equals to 0 degree) usually have higher RCS values.
2) As the distance between the target and the radar plane is getting larger, the RCS value decreases and usually reaches to its minimum at the boundary of radar's vertical FoV.

Based on the characteristics of RCS measurements, the key assumptions are made in this work:

1) Correspondences with higher δ_r should be closer to the radar plane P_r (of elevation angle $\psi = 0$).
2) Correspondences with lower δ_r should be closer to the boundary of the radar's vertical FoV, i.e., upper boundary plane P_U and lower boundary plane P_D,

which are determined by the specification of the radar hardware.

Following the assumptions, the correspondences with higher and lower δ_r's are chosen to refine the 3-DoF parameter set $c_{rcs} = [t_z\ \theta_y\ \theta_x]$. Let δ_V and δ_W be the subset of all correspondences with the highest V% and lowest W% RCS measurement values, respectively. The RCS error term is defined as follows:

$$\varepsilon_{ik} = \begin{cases} d_1, \text{ if } \delta_{rk}(t_i) \in \delta_V \\ d_2, \text{ if } \delta_{rk}(t_i) \in \delta_W \\ 0, \text{ otherwise} \end{cases}, \tag{6}$$

where

$$d_1 = dist({}^r p_{lk}(t_i),\ P_r),$$

$$d_2 = min\{dist({}^r p_{lk}(t_i),\ P_U),\ dist({}^r p_{lk}(t_i),\ P_D)\}.$$

The cost function is defined as the sum of squares of RCS error from $N \times K$ correspondences and the 3-DoF parameter set is obtained by minimizing the cost function using the Ceres Solver [22]:

$$\hat{c_{rcs}} = \arg\min_{c_{rcs}} (\sum_{i=0}^{N-1} \sum_{k=0}^{K-1} \varepsilon_{ik}^2) \tag{7}$$

IV. Temporal Calibration

In this work, the time delay between radar and LiDAR is assumed to be a constant time Δt and temporal calibration can be represented as an estimation problem of the time delay between radar and LiDAR. We estimate this time delay using spatial-temporal relationships of target measurements. As the uncertainty of radar measurements would affect the estimation on the time delay, we argue that sufficient motions on the sensor system are required in this section.

A. Time Delay Estimation

Since the time delay is a one-dimensional parameter, sufficient features in one dimension would be good for the optimization. Thus, aligning the azimuth angle of the target measurements from radar and LiDAR would be sufficient for estimating the time delay. Specifically, the azimuth error term is defined as follows:

$$\epsilon_k(t_i) = |{}^r\phi_{rk}(t_i) - {}^r\ \phi_{lk}(t_i - \delta t)|, \tag{8}$$

where ${}^r\phi_{rk}(t_i)$ is the azimuth angle of the target from radar measurements, and ${}^r\phi_{lk}(t_i - \delta t)$ is the azimuth angle of the target from LiDAR measurements which is transformed into the radar frame by Eq. (3). δt is the estimated value of Δt. Since the ${}^r\phi_{lk}(t)$ is discrete, the intermediate poses are computed using spherical linear interpolation (SLERP).

The time delay is estimated by minimizing the cost function using the Levenberg-Marquardt (LM) algorithm implemented by the Ceres Solver [22]:

$$\delta\tilde{t} = \arg\min_{\delta t} (\sum_{i=0}^{N-1} \sum_{k=0}^{K-1} \epsilon_k^2(t_i)), \tag{9}$$

where the cost function is defined as the sum of squares of azimuth error from $N \times K$ correspondences.

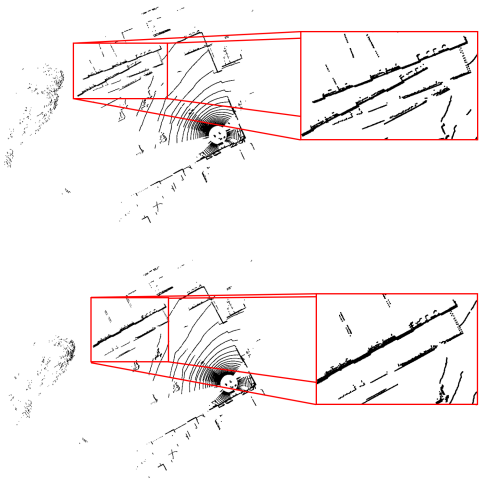

Fig. 5. Comparison of LiDAR measurements before and after LiDAR measurement rectification. (a) The LiDAR scans the same wall twice. The are mismatched wall segments. (b) After rectification, the mismatched problem is resolved.

B. Motion Generation and LiDAR Measurement Rectification

To assess the required sensor motion for temporal calibration, we analyze whether the time delay estimation error would be influenced by the motion. The azimuth error term is rewritten as follows

$$\epsilon_k(t_i) = |{}^r\phi_{rk}(t_i) - {}^r\ \phi_{lk}(t_i - \delta t)| \tag{10}$$

$$= |{}^r\phi_{rk}(t_i) - {}^r\ \hat{\phi}_{lk}(t_i - \delta t)| \tag{11}$$

$$= |{}^r\hat{\phi}_{rk}(t_i) - {}^r\ \epsilon_{rk} - {}^r\ \hat{\phi}_{lk}(t_i - \Delta t) - {}^r\ \omega_{lk}(t_i - \Delta t) \cdot (\Delta t - \delta t)| \tag{12}$$

$$= |{}^r\omega_{lk}(t_i - \Delta t) \cdot (\delta t - \Delta t) - {}^r\ \epsilon_{rk}|, \tag{13}$$

where ${}^r\hat{\phi}_{rk}(t_i)$ is the radar measurement on the azimuth angle without uncertainty, ${}^r\epsilon_{rk}$ is the uncertainty of the radar measurement on the azimuth angle, and the motion ${}^r\omega_{lk}(t_i)$ (i.e., angular velocity) is equal to the derivative of ${}^r\phi_{lk}(t_i)$. Comparing to radar uncertainty, we assume LiDAR uncertainty is small enough to be neglected. Thus, Eq. (11) could be derived and ${}^r\hat{\phi}_{lk}(t_i)$ is defined as the LiDAR measurement on the azimuth angle without uncertainty. Suppose δt is close to Δt, the linear approximation of ${}^r\phi_{lk}(t_i - \delta t)$ can be used in Eq. (12). By definition, ${}^r\hat{\phi}_{rk}(t_i)$ equals ${}^r\hat{\phi}_{lk}(t_i - \Delta t)$ and the terms can cancel out each other. According to Eq. (13), the time delay estimation error $(\delta t - \Delta t)$ could be written as $\frac{{}^r\epsilon_{rk} \pm \epsilon_k(t_i)}{{}^r\omega_{lk}(t_i - \Delta t)}$ which illustrating $(\delta t - \Delta t)$ is inversely proportional to ${}^r\omega_{lk}(t_i - \Delta t)$. When the ${}^r\omega_{lk}(t_i - \Delta t)$ becomes larger, the time delay estimation error would be reduced.

According to the analysis above, rapid motion can both reduce the the time delay estimation error. Thus, we propose to generate motions by moving the sensor system including radar and LiDAR while the targets are stationary. However, LiDAR rectification would be necessary if LiDAR is moved

rapidly. A rectification approach is applied in which the ego-motion is estimated by pairwise scan matching and the transformation of every LiDAR point is estimated by interpolation under an assumption that the motion between two scans is constant and stable. Fig. 5 shows that the LiDAR measurement errors are significantly reduced and the accuracy of localization is also improved.

Once temporal calibration is accomplished, the timestamps of radar measurements in Section III are revised, and the errors caused by the time delay are reduced by iteratively performing extrinsic calibration and temporal calibrations.

V. Experiments

In this section, the experiment setups and results of extrinsic and temporal calibration are described in details.

A. Experiment Setups

A sensor rack equipped with a Velodyne HDL-32E 3D-LiDAR and three Delphi ESR V9.21.15 radars is placed on the top of the vehicle as shown in Fig. 1. The LiDAR frequency is 10 Hz and the radar frequency is 20 Hz. The experiments were conducted in open space as shown in Fig. 3. As Velodyne LiDAR is used in this experiment, it is possible to configure the cut angle to cut the continuous data stream to form the point cloud. The cut angle is set to be 360 degree since LiDAR measurements from all directions are preferred for LiDAR localization. The calibration target is a corner reflector with a triangular styrofoam board fixed in front. The center of the reflector and the styrofoam board are aligned as shown in Fig. 4. A plastic tube and a plastic base are used as the target stand since plastic materials reflect back signals with weaker radar echo intensity compared with corner reflector. Therefore, performing RCS thresholding is used to avoid misinterpreting the target stand for the actual target.

In the data collection process, the software is run on Robot Operating System (ROS), and the timestamps of all sensor measurements are generated by the computer's system clock. The additional delays from communication, the operating system and ROS could occur. We assume those delays are summed to be a constant and the uses of the timestamps from sensor clocks to further improve temporal calibration performance would be our future work.

1) Extrinsic Calibration Data Collection Procedures: To ensure the accuracy of extrinsic calibration, the targets are placed at 7 different heights and adjusted to point towards radar at the beginning. To alleviate the effort in data collection, the data were collected continuously by driving the vehicle away from the targets up to 10 m in different moving directions as shown in Fig. 3(a). As radar's azimuth accuracy would induce larger reprojection error at long-range and would cause more uncertainty on x-translation and y-translation, the calibration targets were not located more than 10 m away. While the calibration performance depends on the quality of RCS measurements, the extrinsic calibration results following the proposed data collection procedures show its effectiveness in Section V-B as the collected data still follows the RCS distribution rules. In addition, the vehicle was driven slowly to reduce the influence of the time delay between the radars and the LiDAR and the error caused by the time delay can be further compensated via the proposed temporal calibration procedures.

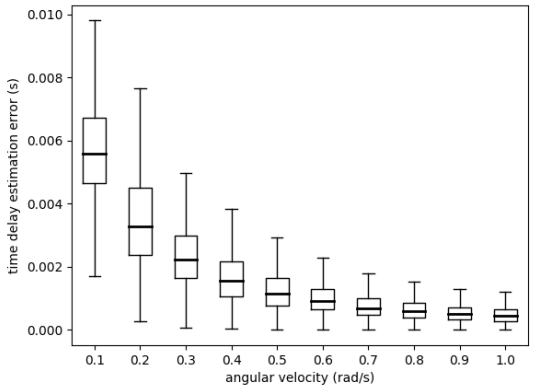

Fig. 6. The box plot shows the time delay estimation errors for different angular velocities in simulation. The result shows that the error median decreases and the distribution becomes more certain with higher angular velocities.

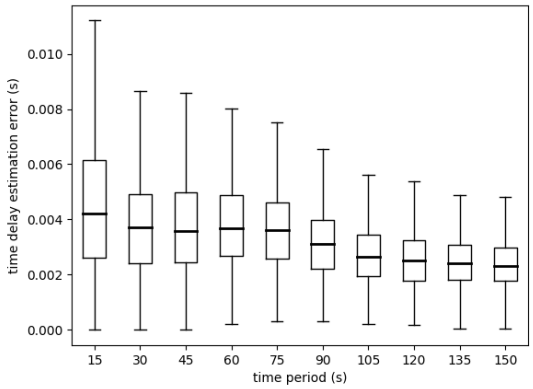

Fig. 7. The box plot show the time delay estimation errors from different time periods in simulation. The result shows that the error median decreases and the distribution becomes more certain with longer time period of measurements.

2) Temporal Calibration Data Collection Procedures: Two calibration targets were placed at 9.44 meter and 20.12 meter away from the sensor system as shown in Fig. 3(b). As the radar and LiDAR were mounted firmly on the sensor rack, sufficient motions can be easily generated by moving the sensor rack directly.

To assess the motion required for temporal calibration, two simulations are performed. In the simulations, the data were generated based on the specifications of radar and LiDAR, and our experiment setup. Both simulations were run 1000 times. In the first simulation, the target trajectories were generated by different angular velocities of the sensor rack in a fixed time period, 30 seconds. In the second simulation, the target trajectories were generated by different time periods

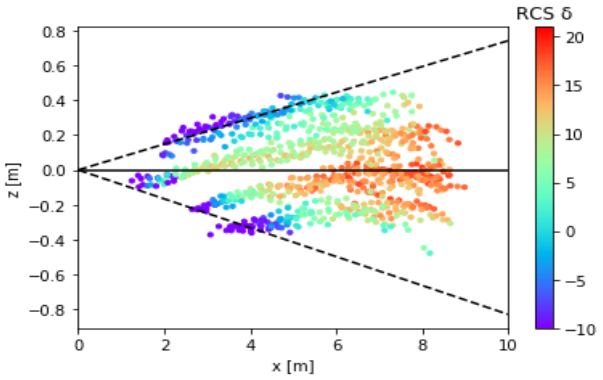

Fig. 8. RCS distribution across transformed LiDAR data in radar's FoV. The LiDAR data is colored based on the RCS value of paired radar measurement. Solid line: Radar plane; Dashed line: Boundary of radar's vertical FoV.

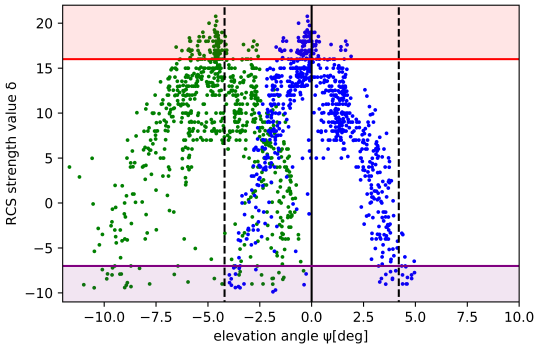

Fig. 9. RCS distribution with respect to the pitch angle. Correspondences with higher RCS value (above the red line) and with lower RCS value (below the purple line) are used for optimization. Green points: After reprojection error optimization; Blue points: After RCS error Optimization; Black dashed line: The boundary of vertical FoV.

with a fixed angular velocity, 0.3 rad/s. Fig. 6 and Fig. 7 show that higher angular velocity and longer time period would reduce the time delay estimation error in which our inference in Sec. IV-B is confirmed. According to the simulation result, we kept the angular velocity over one radian per second The time for data collection is around 30 seconds. The motion of the sensor rack was generated by that two people hold each side of the sensor rack and rotate the sensor rack as stable and rapid as possible. For obtaining the motion ground truth and improving motion generation, a mechanical device such as a vehicle turntable would be a more desirable choice.

B. Results

1) Extrinsic Calibration Results: In order to verify the performance of the estimated extrinsic calibration parameters, three analyses were conducted.

First, the two-stage optimization is accomplished and the calibration results for reprojection error optimization $\hat{c_p}$, RCS error optimization $\hat{c_{rcs}}$, carefully tape measured translation ${}^r\tilde{t}_l$ are listed below:

- $\hat{c_p} = [0.16\ m,\ 0.11\ m,\ 0.07\ m,\ 35.1°, -0.4°, -5.0°]$
- $\hat{c_{rcs}} = [0.26\ m,\ 2.6°,\ -0.6°]$
- ${}^r\tilde{t}_l = [0.15\ m,\ 0.1\ m,\ 0.27\ m]$

We can observe that there are slight differences between estimated parameters in translation and tape measurements. The differences could originate from the imprecision in tape measurements and the limits of accuracy in radar measurement ($\pm 0.25\ m$ for range accuracy; $\pm 1°$ for azimuth accuracy [23]). After reprojection error optimization, the average reprojection error, i.e., the average Euclidean distance between radar data and projected LiDAR data is about $0.074\ m$, which is below the range accuracy of Delphi radar.

Second, to examine the RCS distribution in radar's vertical FoV, LiDAR measurements are transformed into the radar frame by applying the estimated extrinsic parameters. The spatial distribution of LiDAR data in the lateral view is plotted in Fig. 8, where LiDAR measurements are colored according to the RCS values of paired radar measurements. We can observe that RCS value decreases as the distance between the target measurement and the radar plane is getting larger, and reach its minimum at the boundary planes. The boundary planes are the planes with $+4.5°$ and $-4.5°$ elevation angle, which are determined by the specification of Delphi radar [23]. Fig, 9 shows the relation between RCS value and the elevation angle of transformed LiDAR data. After reprojection error optimization, plenty of target measurements are still located outside radar's vertical FoV. On the other hand, the distribution is significantly improved after RCS error optimization.

	Reprojection Error Optimization	RCS Error Optimization
$t_x[m]$	$N(0.158, 2.417 \times 10^{-4})$	—
$t_y[m]$	$N(0.110, 4.917 \times 10^{-4})$	—
$t_z[m]$	$N(0.116, 1.141 \times 10^{-1})$	$N(0.262, 4.198 \times 10^{-5})$
$\theta_z[°]$	$N(35.699, 4.208 \times 10^{-2})$	—
$\theta_y[°]$	$N(-0.744, 7.590 \times 10^{-0})$	$N(2.577, 2.424 \times 10^{-3})$
$\theta_x[°]$	$N(-4.282, 1.319 \times 10^{-0})$	$N(-0.580, 1.265 \times 10^{-4})$

TABLE I
CALIBRATION RESULT OF TWO-STAGE OPTIMIZATION

Finally, we performed Monte Carlo experiments for 1000 runs by randomly sub-sampling all the correspondences into half of the original number. Compared with other parameters, Table I shows that t_z, θ_y, θ_x have larger variances and required to be refined in RCS error optimization. Fig. 10 presents the distribution of t_z, θ_y, θ_x after two optimizations. After RCS error optimization, the three parameters' variances are significantly reduced, the mean values are changed as well. The mean of t_z estimation become closer to tape measured value.

For the purpose of comparison, the method suggested in [13] which resembles RCS-elevation relation as one parabola curve has been implemented, labelled as method *RCS*. The results of our proposed method and Method *RCS* are shown in Table II. While there could be no significant differences between the proposed method and Method *RCS*, we argue

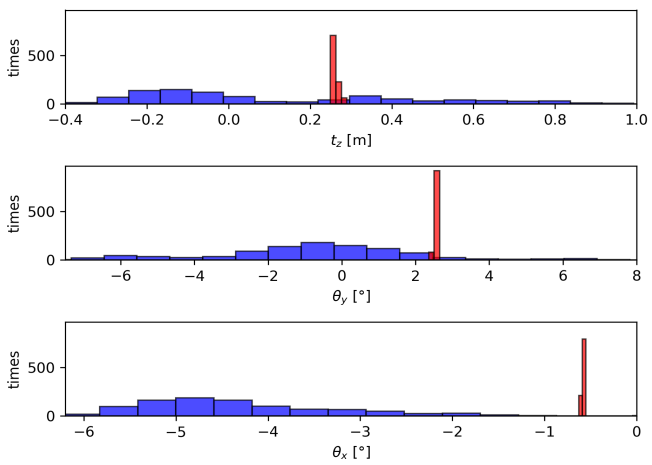

Fig. 10. Monte Carlo Analysis: the distribution of estimated extrinsic parameters. Blue: After Reprojection Error Optimization; Red: After RCS Error Optimization.

	Proposed method	RCS [13]
$t_z[m]$	$N(0.262, 4.198 \times 10^{-5})$	$N(0.237, 7.711 \times 10^{-7})$
$\theta_y[°]$	$N(2.577, 2.424 \times 10^{-3})$	$N(2.703, 2.176 \times 10^{-5})$
$\theta_x[°]$	$N(-0.580, 1.265 \times 10^{-4})$	$N(-0.833, 1.345e \times 10^{-4})$

TABLE II

MONTE CARLO ANALYSIS RESULTS FOR RCS ERROR OPTIMIZATION

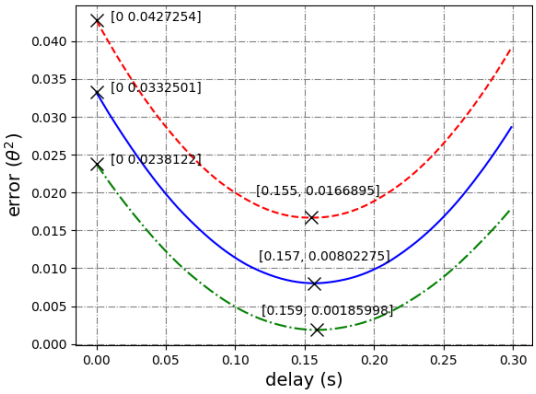

Fig. 11. Results of error calculation between three radars. Red line: The left radar; Blue line: The middle radar; Green line: The right radar.

that the RCS distribution may not be well represented by a parabola curve based the observations on the collected radar measurements.

2) Temporal Calibration Results: Fig. 11 shows that the time delays from three radars are around 0.16 second. After temporal calibration, the mean-square error of azimuth angle has 60% to 90% decrease. The total number of samples is around 2000 radar measurements in which the reliability of the approach is validated.

After the time delay is estimated, the timestamps of the radar measurements can be revised and be examined as shown in Fig. 13 in which the initial and modified alignments

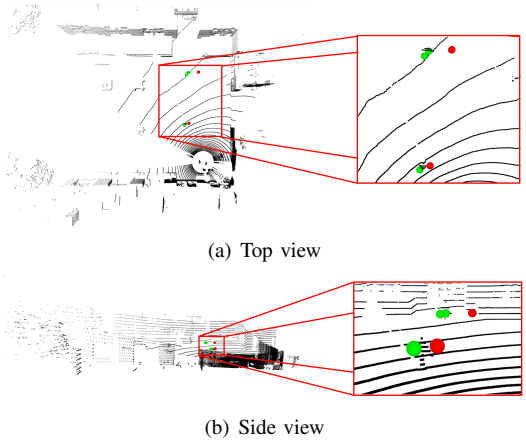

(a) Top view

(b) Side view

Fig. 12. Comparison of before and after temporal calibration. Red point: Before temporal calibration; Green point: After temporal calibration.

of the estimated target azimuth angles from the radars and the LiDAR are shown in which the temporal calibration performance is demonstrated. In addition, we compare radar and LiDAR measurements in the same frame to verify the effectiveness of temporal calibration. After temporal calibration, the average distance between radar data and LiDAR data decreases from 1.78 meter to 0.94 meter for the near target, and from 3.8 meter to 2.01 meter for the farther target. Fig. 12 illustrates that the radar measurements are close to LiDAR measurements after temporal calibration.

VI. CONCLUSION AND FUTURE WORK

The approaches to estimate the extrinsic parameters and the time delay between planar radars and a 3D-LiDAR have been presented. Based on the characteristics of planar radar RCS distribution in 3D space, the extrinsic parameters are estimated and used for temporal calibration. A target-based approach to estimate the time delay between planar radar and 3D LiDAR has been demonstrated and verified. To the best of our knowledge, our approach is the first one to accomplish both extrinsic and temporal calibrations of automotive radars and LiDARs.

The experiment results show there is small time delay drift for three radars. It would be our plan to perform more experiments to analyze the influence factors of time delay estimation. As sufficient motions during data collection are required for temporal calibration but these motions could make extrinsic calibration less reliable. In this work, extrinsic and temporal calibrations are not performed simultaneously. Further improvements on optimization and integration of both calibration tasks would be our future work.

ACKNOWLEDGEMENT

This work was supported in part by Industrial Technology Research Institute (ITRI), Ministry of Economic Affairs (MOEA) in Taiwan, and by grants from Ministry of Science and Technology (MOST) in Taiwan (#109-2221-E-009-119-MY3, #109-2221-E-009-120-MY3).

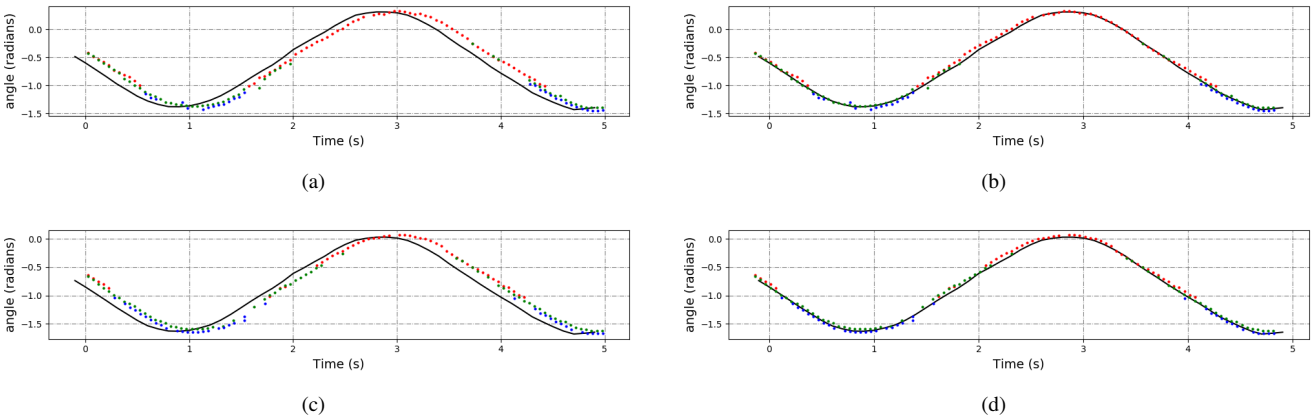

Fig. 13. Comparison of target azimuth angle alignments. The black curve is estimated by LiDAR, The red, green and blue points are estimated by the three on-board automotive radars respectively. The top row is from near target and the bottom row is from farther target. The left column shows the alignments mismatching before temporal calibration. The right column shows the azimuth angle measurements from each sensor matching together after temporal calibration.

REFERENCES

[1] C. Le Gentil, T. Vidal-Calleja, and S. Huang, "3D Lidar-IMU Calibration based on Upsampled Preintegrated Measurements for Motion Distortion Correction," in *Proceedings of IEEE International Conference on Robotics and Automation (ICRA)*, 2018.

[2] J. Castorena, U. S. Kamilov, and P. T. Boufounos, "Auto calibration of LiDAR and optical cameras via edge alignment," in *Proc. IEEE Int. Conf. Acoust. Speech Signal Process. (ICASSP)*, March, 2016, pp. 2862–2866.

[3] J. Levinson and S. Thrun, "Automatic Online Calibration of Cameras and Lasers," in *Proceedings of the Robotics: Science and Systems*, 2013.

[4] J. Jeong, L. Y. Cho, and A. Kim, "Road is Enough! Extrinsic Calibration of Non-overlapping Stereo Camera and LiDAR using Road Information," *arXiv preprint arXiv:1902.10586*, 2019.

[5] Y. Park, S. Yun, C. S. Won, K. Cho, K. Um, and S. Sim, "Calibration between Color Camera and 3D LIDAR Instruments with a Polygonal Planar Board," *Sensors*, vol. 14, no. 3, pp. 5333–5353, 2014.

[6] A. Dhall, K. Chelani, V. Radhakrishnan, and K. M. Krishna, "LiDAR-Camera Calibration using 3D-3D Point correspondences," *arXiv preprint arXiv:1705.09785*, 2017.

[7] C. Guindel, J. Beltrán, D. Martín, and F. García, "Automatic Extrinsic Calibration for Lidar-Stereo Vehicle Sensor Setups," in *IEEE International Conference on Intelligent Transportation Systems (ITSC)*, 2017.

[8] T. Wang, N. Zheng, J. Xin, and Z. Ma, "Integrating millimeter wave radar with a monocular vision sensor for on-road obstacle detection applications," *Sensors*, vol. 11, no. 9, pp. 8992–9008, 2011.

[9] J. Oh, K.-S. Kim, M. Park, and S. Kim, "A Comparative Study on Camera-Radar Calibration Methods," in *International Conference on Control, Automation, Robotics and Vision (ICARCV)*, 2018.

[10] C. Schöller, M. Schnettler, A. Krämmer, G. Hinz, M. Bakovic, M. Güzet, and A. Knoll, "Targetless Rotational Auto-Calibration of Radar and Camera for Intelligent Transportation Systems," *arXiv preprint arXiv:1904.08743*, 2019.

[11] S. Sugimoto, H. Tateda, H. Takahashi, and M. Okutomi, "Obstacle Detection Using Millimeter-wave Radar and Its Visualization on Image Sequence," in *Proceedings of the 17th International Conference on Pattern Recognition (ICPR)*, 2004, pp. 342–345.

[12] J. Peršić, I. Marković, and I. Petrović, "Extrinsic 6Dof Calibration of 3D LiDAR and Radar," in *European Conference on Mobile Robotics (ECMR)*, 2017, pp. 165–170.

[13] J. Peršić, I. Marković, and I. Petrović, "Extrinsic 6dof calibration of a radar–lidar–camera system enhanced by radar cross section estimates evaluation," *Robotics and Autonomous Systems*, vol. 114, pp. 217–230, 2019.

[14] F. M. Mirzaei and S. I. Roumeliotis, "A Kalman Filter-Based Algorithm for IMU-Camera Calibration: Observability Analysis and Performance Evaluation," *IEEE Transactions on Robotics*, vol. 24, no. 5, pp. 1143–1156, 2008.

[15] M. Li and A. I. Mourikis, "3-D motion estimation and online temporal calibration for camera-IMU systems," in *IEEE International Conference on Robotics and Automation*, 2013, pp. 5709–5716.

[16] M. Fleps, E. Mair, O. Ruepp, M. Suppa, and D. Burschka, "Optimization based IMU camera calibration," in *IEEE/RSJ International Conference on Intelligent Robots and Systems*, 2011, pp. 3297–3304.

[17] J. Kelly and G. S. Sukhatme, "A General Framework for Temporal Calibration of Multiple Proprioceptive and Exteroceptive Sensors," in *Experimental Robotics*, 2014, pp. 195–209.

[18] J. Kelly, N. Roy, and G. S. Sukhatme, "Determining the Time Delay Between Inertial and Visual Sensor Measurements," *IEEE Transactions on Robotics*, vol. 30, no. 6, pp. 1514–1523, 2014.

[19] A. Segal, D. Haehnel, and S. Thrun, "Generalized-icp," in *Robotics: science and systems*, 2009, p. 435.

[20] P. Biber and W. Straßer, "The normal distributions transform: A new approach to laser scan matching," in *Proceedings 2003 IEEE/RSJ International Conference on Intelligent Robots and Systems (IROS 2003)(Cat. No. 03CH37453)*, vol. 3. IEEE, 2003, pp. 2743–2748.

[21] E. Meijering, "A chronology of interpolation: from ancient astronomy to modern signal and image processing," *Proceedings of the IEEE*, vol. 90, no. 3, pp. 319–342, 2002.

[22] S. Agarwal, K. Mierle, and Others, "Ceres Solver," http://ceres-solver.org, 2016.

[23] L. Stanislas and T. Peynot, "Characterisation of the Delphi Electronically Scanning Radar for Robotics Applications," in *Proceedings of the Australasian Conference on Robotics and Automation*, 2015.